

https://doi.org/10.1070/QEL17512

Prospects for multimodal visualisation of biological tissues using fluorescence imaging

D.K. Tuchina, I.G. Meerovich, O.A. Sindeeva, V.V. Zherdeva, N.I. Kazachkina, I.D. Solov'ev, A.P. Savitsky, A.A. Bogdanov Jr., V.V. Tuchin

Abstract. **We investigate skin optical clearing in laboratory animals *ex vivo* and *in vivo* by means of low-molecular-weight paramagnetic contrast agents used in magnetic resonance imaging (MRI) and a radiopaque agent used in computed tomography (CT) to increase the sounding depth and image contrast in the methods of fluorescence laser imaging and optical coherence tomography (OCT). The diffusion coefficients of the MRI agents Gadovist®, Magnevist®, and Dotarem®, which are widely used in medicine, and the Visipaque® CT agent in *ex vivo* mouse skin, are determined from the collimated transmission spectra. MRI agents Gadovist® and Magnevist® provide the greatest optical clearing (optical transmission) of the skin, which allowed: 1) an almost 19-fold increase in transmission at 540 nm and a 7–8-fold increase in transmission in the NIR region from 750 to 900 nm; 2) a noticeable improvement in OCT images of skin architecture; and 3) a 5-fold increase in the ratio of fluorescence intensity to background using TagRFP-red fluorescent marker protein expressed in a tumour, after application to the skin of animals *in vivo* for 15 min. The obtained results are important for multimodal imaging of tumours, namely, when combining laser fluorescence and OCT methods with MRI and CT, since the contrast agents under study can simultaneously enhance the contrast of several imaging methods.**

D.K. Tuchina Saratov State University, ul. Astrakhanskaya 83, 410012 Saratov, Russia; National Research Tomsk State University, prosp. Lenina 36, 634050 Tomsk, Russia; Bach Institute of Biochemistry, Federal Research Centre 'Fundamentals of Biotechnology', Russian Academy of Sciences, Leninsky prosp. 2, stroenie 33, 119071 Moscow, Russia;
I.G. Meerovich, V.V. Zherdeva, N.I. Kazachkina, I.D. Solov'ev, A.P. Savitsky Bach Institute of Biochemistry, Federal Research Centre 'Fundamentals of Biotechnology', Russian Academy of Sciences, Leninsky prosp. 2, stroenie 33, 119071 Moscow, Russia;
O.A. Sindeeva Saratov State University, ul. Astrakhanskaya 83, 410012 Saratov, Russia;
A.A. Bogdanov Jr. Bach Institute of Biochemistry, Federal Research Centre 'Fundamentals of Biotechnology', Russian Academy of Sciences, Leninsky prosp. 2, stroenie 33, 119071 Moscow, Russia; University of Massachusetts Medical School, 55 N Lake Ave, Worcester, MA 01655, United States;
V.V. Tuchin Saratov State University, ul. Astrakhanskaya 83, 410012 Saratov, Russia; National Research Tomsk State University, prosp. Lenina 36, 634050 Tomsk, Russia; Bach Institute of Biochemistry, Federal Research Centre 'Fundamentals of Biotechnology', Russian Academy of Sciences, Leninsky prosp. 2, stroenie 33, 119071 Moscow, Russia; Institute of Precision Mechanics and Control, Russian Academy of Sciences, ul. Rabochaya 24, 410028 Saratov, Russia; e-mail: tuchinvv@mail.ru

Received 21 December 2020
Kvantovaya Elektronika **51** (2) 104–117 (2021)
Translated by V.L. Derbov

Keywords: *optical tomography, OCT, MRI, CT, optical clearing, contrast MRI and CT agents, skin of laboratory animals, in vivo, ex vivo.*

1. Introduction

X-ray computed tomography (CT), magnetic resonance imaging (MRI) or optical tomography are commonly used to study the 3D structure of pathologies in biological tissues and organs. The optical tomography is based on various laser techniques, such as diffuse reflection, fluorescence imaging, photoacoustic and optical coherence tomography (OCT), which provide information about the structure and functions of tissues and organs [1–4]. The use of multimodal biomedical imaging is often the key to understanding physiological processes, as well as a tool for monitoring disease progression and optimising treatment. Multimodal concepts combining the strengths of various imaging technologies [1, 2] are expected to help in obtaining high-quality optical image reconstruction. Modern methods of tomographic clinical imaging, such as CT and MRI, are being permanently modernised to use new and more effective contrast agents [5]. In general, medical optical imaging methods provide high spatial resolution, speed, and specific molecular contrast [2–4]. However, they generally have limited probing depth and field of view.

Strong light scattering significantly complicates optical imaging of tissues and organs [3, 4]. Recent advances in reducing the effect of scattering of the probing and detected laser beams on obtaining high-contrast optical images are associated with the development and application of a new methodology for immersion optical clearing (OC) of tissues [3, 4, 6–32]. OC is based on the temporary and reversible equalisation of the refractive indices of solid components of tissue and interstitial fluid to reduce structural inhomogeneity and, accordingly, strong light scattering, by using immersion solutions – optical clearing agents (OCAs).

Various biocompatible agents have been successfully used for *in vitro*, *ex vivo* and *in vivo* studies, alone or in combination with traditional chemical or physical enhancers commonly used to deliver drugs through biological membranes, especially through the eye sclera, dura mater and skin [6–10, 14, 17, 23, 27, 29, 30]. Recently, a number of more complex OCAs have been developed for application to fixed tissues with preliminary fluorescent labelling [11–16]. These multicomponent agents include 3DISCO, uDISCO, FDISCO, SeeDB, ScaleS, Clear T2, PACT, FASTClear, and CUBIC [11–16, 18–22, 24–28, 31, 32]. All of them are successfully used for three-dimensional imaging of various organs, includ-

ing the brain, as well as the entire body of small animals. However, it takes a long time (hours and days) for volumetric clearing of fixed tissues; therefore, such methods cannot be used in *in vivo* studies.

It is important to note that some CT contrast agents (Omnipaque®, Trazograph®, Hypaque®, Urografin®, etc.) improve the optical transparency of the eye sclera, skin, cartilage tissue and some other tissues [6, 8–10, 20, 23, 30–35]. Since CT agents are well studied as effective OCAs [8, 20, 34–37], a combination of CT and optical imaging is possible.

The combination of optical imaging and MRI is also potentially relevant for multimodal imaging. Any OCA must be biocompatible, and many MRI agents are already widely used in clinical practice [38–41]. By the end of 2009, the number of doses of MRI agents used in the United States was estimated at 87.5 million [40]. For this study, Gadovist®, Magnevist®, and Dotarem® were selected, i.e. agents containing paramagnetic gadolinium (Gd^{3+}), which has the largest number of unpaired electrons among all stable ions (seven) and creates a high electron spin moment, effective for enhancing proton relaxation [38–40]. Of these agents, Magnevist® was developed in 1988 and further distributed in many regions of the world. In the USA, the macrocyclic non-ionic agent Gadovist® was approved in 2011, and the macrocyclic ionic agent Dotarem®, in 2013 [41]. Recently, the clinically approved iodine-based isoosmolar CT agent Visipaque® has been proposed as an MRI agent [42]. Based on it, an approach was developed for bimodal CT/MRI imaging to monitor the delivery and biodistribution of liposomes loaded with Visipaque®.

It should be noted that the potential of multimodal imaging is highly dependent on the spatial resolution of each of the methods involved, as well as on the time required to obtain an image. Optical methods such as OCT and laser fluorescence provide subcellular resolution of several microns with an image acquisition rate from tens of frames per second to one frame in a few minutes [1–4]. The spatial and temporal resolution of preclinical MRI and micro-CT is at least 10 times lower. These methods ensure a comparable spatial resolution of 125 μm for in-plane MRI images and 88 μm for isotropic resolution micro-CT for an animal model of cancer [43]. However, the 'anatomical' resolution of MRI is highly dependent on many variables, and even with the most comparable imaging modes, such as using fast MR pulses, imaging can take up to 5 times longer than micro-CT. Thus, when using additional multimodal approaches, the specifics of each of them should be taken into account.

In the present study, we obtained and analysed the time-dependent optical transmission and OCT images of *ex vivo* laboratory mice skin samples exposed to MRI and CT contrast agents (Gadovist®, Magnevist®, Dotarem® and Visipaque®). Using on the data obtained, the diffusion coefficients of these agents were found, which made it possible to elaborate the research protocol for *in vivo* measurements of pulsed laser-excited fluorescence images of labelled tumour cells with topical application of the most efficient agent (Gadovist®) to the surface of the animal's skin. These studies prove the efficacy of using contrast CT and MRI agents for OC in the context of multimodal MRI/CT/optical tissue imaging.

2. Materials

Optical measurements were performed using the *ex vivo* skin of inbred white mice (Saratov State Medical University, Russia) and Nu/Nu hairless mice (Federal Research Centre 'Fundamentals of Biotechnology' of the Russian Academy of Sciences, Moscow, Russia). Skin samples (10 × 15 mm) were obtained by biopsy from white mice after hair removal with depilatory cream. Before the measurements, the subcutaneous fat layer was also removed with tweezers as much as possible to allow the free OCA diffusion through the dermal layer of the skin. For all *ex vivo* studies, the sample thickness was measured with a digital micrometer (Fujisan, China) with an accuracy of ~1 μm before and after saturation of the skin sample with a contrast MRI or CT agent used as an OCA, and the data were averaged over three to five measurements for each sample. The Ethics Committee of Saratov State Medical University (Protocol No. 8 dated April 10, 2018) approved animal studies.

In OC experiments, Gadovist® (1.0 mmol mL^{-1}) and Magnevist® (0.5 mmol mL^{-1}) (Bayer HealthCare Pharmaceuticals, Germany), as well as Dotarem® (0.5 mmol mL^{-1}) (Guerbet, France) were used. Saline served for a control solution.

To prove the concept of three-modal imaging of biological tissue based on the simultaneous use of MRI, CT and optical methods, an iodine-containing isoosmolar X-ray contrast agent iodixanol (1550.2 g mol^{-1}) with an iodine concentration of 270 mg mL^{-1} (Visipaque®, GH Healthcare, Chicago, Illinois, USA) was used.

To quantify the potential of MRI and CT contrast agents as an OCA, the refractive indices of the agents and control saline were measured using an Abbe DRM2/1550 multiwave refractometer (ATAGO, Japan) in the range of 450–1550 nm at a temperature of 22.4 ± 1.1 °C. The refractometer measurement accuracy is ±0.0002 refractive index units. Refractive indices were measured three times for twelve wavelengths (Fig. 1).

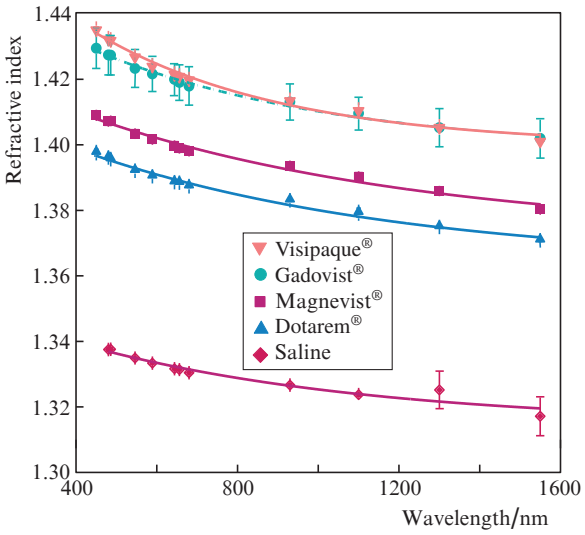

Figure 1. Wavelength dependences of refractive indices of MRI and CT contrast agents, as well as saline solution.

3. Visualisation of the test object and OCT measurements

Digital visualisation of the test object and OCT measurements were performed using *ex vivo* white mouse skin sam-

ples. Each sample was photographed with a camera equipped with a colour CMOS sensor IMX286 (Sony) with a resolution of 3968 × 2976 (12 megapixels) to register different degrees of transparency of optically cleared skin in the U-zone (a section of the lettering 'SSU' printed using a laser printer on a sheet of white paper placed immediately behind the biotissue sample). Then, images were obtained in the form of B-scans using a Spectral Radar OCT system (OCP930SR 022, Thorlabs Inc., USA) operating at a wavelength of 930 nm with a spectral band of 100 nm and an output power of the radiation beam of 2 mW. The scanning depth and longitudinal spatial resolution in air were 1.6 mm and 6.2 μm, respectively, and the transverse spatial resolution was 8 μm [44]. OCT images of the skin were recorded from the side of the epidermis surface of each sample before and after 30 and 60 minutes of immersion in agent solutions or saline (control). Skin samples were immersed in Petri dishes with agents completely covering them.

After obtaining the mean grayscale values of the black character U (I_{min}) and the white area (I_{max}) located under the skin sample, using the ImageJ package (NIH, USA) for digital image analysis, the image contrast K was calculated before and after the action of the agents:

$$K = \frac{I_{max} - I_{min}}{I_{max} + I_{min}}. \quad (1)$$

Digital images of the U-zone were obtained for three MRI agents (Gadovist®, Magnevist® and Dotarem®) and CT agent (Visipaque®), as well as saline, before immersing the tissue sample in the agent and in 30 and 60 minutes after the immersion. The results shown in Fig. 2 allow a visual assessment of the OC effect. Skin samples become visually clearer, with the most pronounced effect observed for Gadovist®.

The average values and standard deviations of the image contrast enhancement after 30 and 60 min of MRI and CT agents or saline solution acting on the murine skin (Table 1) were determined from the images in Fig. 2 as a ratio of contrast after 30 and 60 min of immersion to the contrast before the immersion.

Figure 3 shows *ex vivo* OCT B-scans of mouse skin samples before and after 30 and 60 min immersion in OCA solutions. The sample thickness values measured with a digital micrometer before and after immersion in these solutions are shown in Table 2.

Figure 4 shows typical dependences of the OCT signal on the optical probing depth of the mouse skin before and after the sample immersion in the Gadovist® solution. A decrease in the slope of the dependence of the magnitude of the OCT signal on depth and an increase in the signal at great depths (Fig. 4b) with an increase in the immersion time in this solution, which is due to a decrease in scattering in the upper layers of the skin [3].

After immersion of the skin in a solution of an MRI or CT agent, the OCT scan shows less scattering of light in the skin samples (Figs 3, 4). In the case of immersion in saline, the opposite effect was observed, i.e., a slight increase in scattering. Compared with saline, the action of contrast agents leads to the appearance of a more detailed structure of the skin and subcutaneous adipose tissue on OCT images. The possibility of observing a finer tissue structure arose after 30 and 60 minutes of exposure to all studied contrast agents, but to a different extent. At the same time, the depth of tissue sounding increased.

The sample thickness l, measured with a micrometer (Table 2), correspond to the OCT data (see Fig. 3), taking into account the values of the average refractive index n of the tissue samples, since OCT actually measures the optical path length nl. Note that one should expect some increase in n values caused by the penetration of agents with a higher refractive index (see Fig. 1) than in the interstitial medium (interstitial fluid), n = 1.34–1.35 [3], and some dehydration upon exposure to Magnevist® and Visipaque® agents (Table 2). No change in skin thickness was observed within 60 minutes after

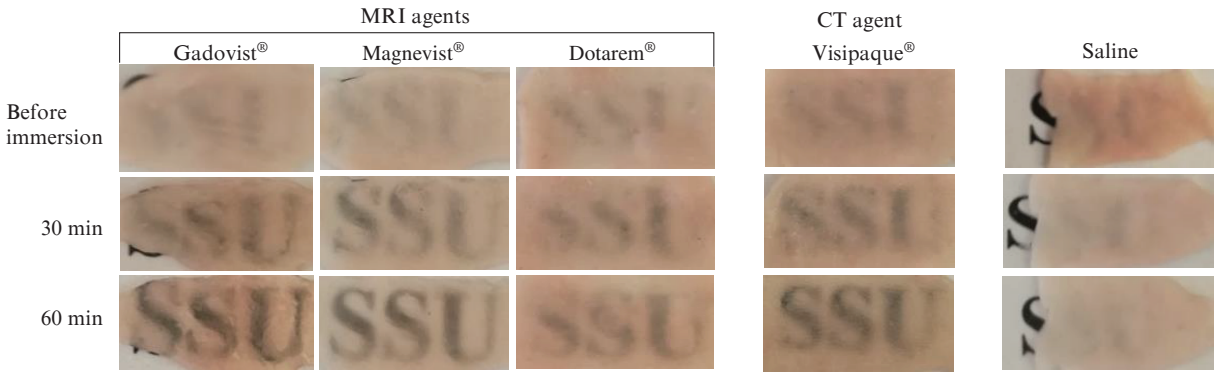

Figure 2. Digital images of a test object located behind white mouse skin samples exposed to Gadovist®, Magnevist®, Dotarem®, Visipaque® and saline: before immersion, 30 and 60 minutes after immersion of the sample in solution.

Table 1. Mean values and standard deviations of the multiplicity of the increase in the contrast of images after 30 and 60 min of exposure of skin of white mice to MRI and CT agents or saline.

Time/min	MRI agents			CT agent	Saline
	Gadovict®	Magnevist®	Dotarem®	Visipaque®	
30	1.9 ± 0.8	2.0 ± 1.0	2.0 ± 0.6	1.4 ± 2.2	0.6 ± 0.4
60	4.4 ± 1.9	4.9 ± 1.7	2.8 ± 0.4	2.2 ± 2.9	0.7 ± 0.2

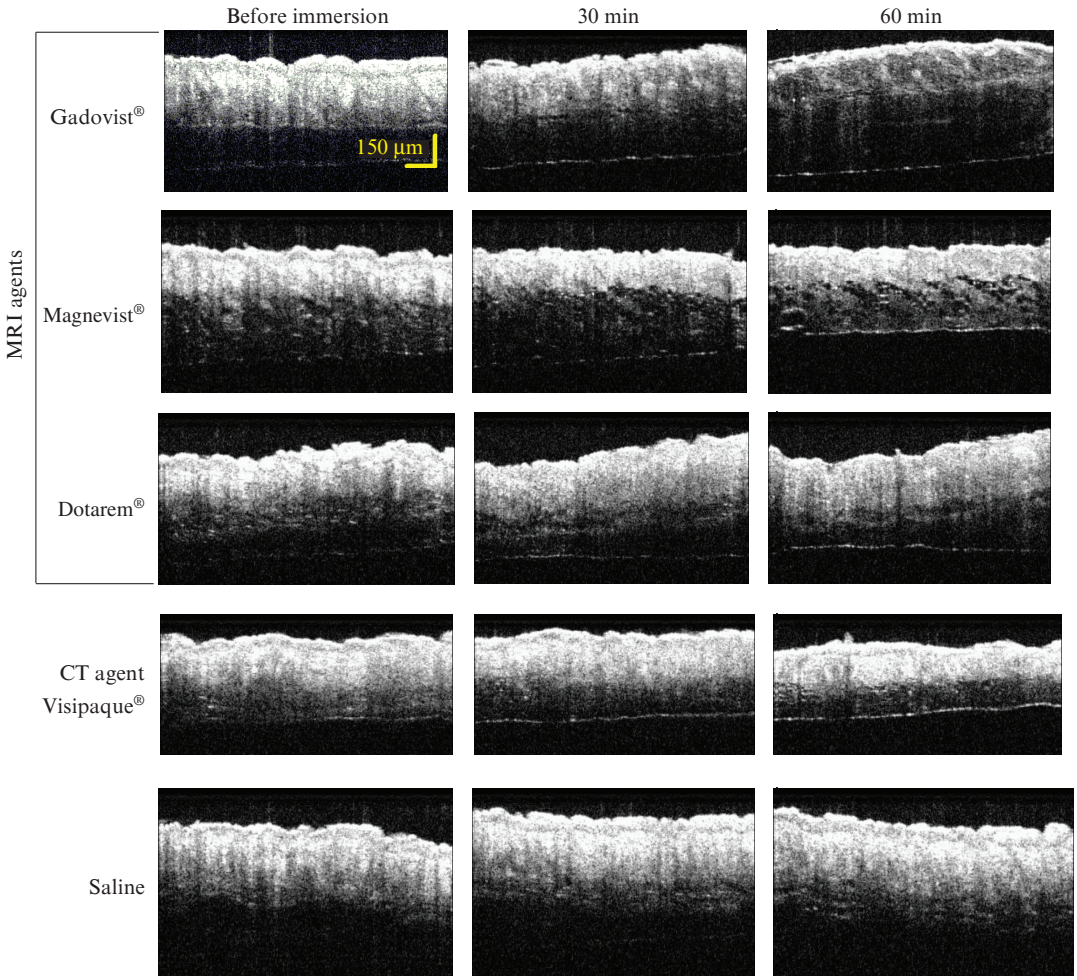

Figure 3. B-scans of OCT [–1g(*R*)] *ex vivo* skin samples of white mice before and after 30 and 60 min immersion in solutions of contrasting MRI and CT agents, as well as in saline (control).

Table 2. Mean values and standard deviations of thickness *l* (mm) of skin samples used in digital (Fig. 2) and OCT imaging (Figs 3, 4) before and after 60-min immersion in MRI and CT agents or in saline.

Time/min	MRI agents			CT agents	Saline
	Gadovict®	Magnevist®	Dotarem®	Visipaque®	
Before immersion	0.31 ± 0.02	0.32 ± 0.03	0.26 ± 0.04	0.33 ± 0.07	0.32 ± 0.02
60	0.31 ± 0.02	0.27 ± 0.07	0.28 ± 0.04	0.27 ± 0.07	0.34 ± 0.02

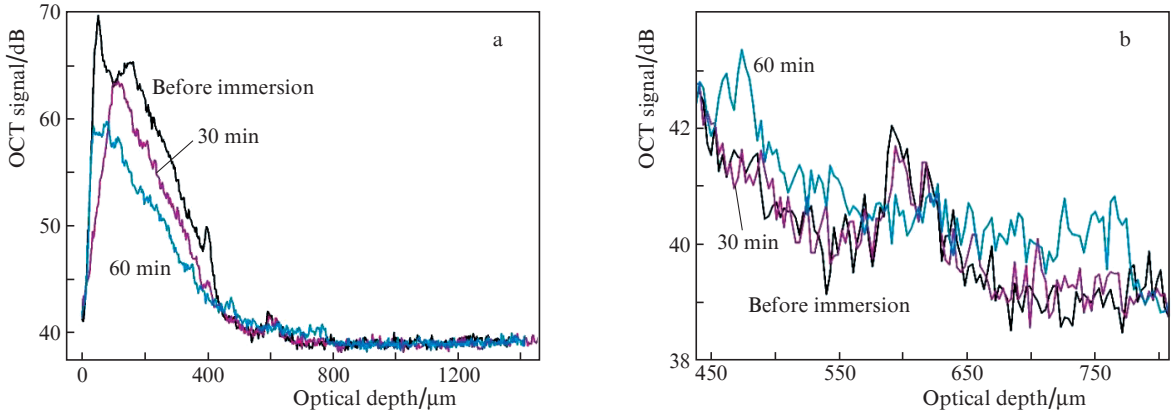

Figure 4. (Colour online) Typical dependences of the OCT signal on the optical depth of probing of the mouse skin before and after 30 and 60 min immersion of the sample in the Gadovist® solution (a), as well as the scaled up OCT signal in the depth range of 440–810 μm (b).

immersion of the samples in Gadovist®, while Magnevist® and Visipaque® caused some reduction in skin thickness (transverse shrinkage). Conversely, the use of the Dotarem® MRI agent, which has a high water content, or saline results in some tissue swelling.

4. Spectral measurements of collimated transmittance

For spectral measurements of collimated transmittance, skin samples from hairless Nu/Nu and white mice were used. Each skin sample was fixed on a plastic plate with a hole in the centre for light passage. The plate was placed in a glass cuvette with OCA or saline. The cuvette with the sample was placed between two QP400-1-UV-VIS optical fibres (Ocean Insight, USA) with a core diameter of 400 μm and 74-ACR collimators (Ocean Insight, USA). A HL-2000 halogen lamp (Ocean Insight, USA) was used as a light source. All measurements were performed at room temperature (~25 °C). The collimated transmission spectra of skin were recorded every 30 or 60 s for 60 min using a USB4000-Vis-NIR multichannel spectrometer (Ocean Insight, USA) (Fig. 5) [45] in the wavelength range of 500–900 nm. For noise correction, the MATLAB® R2018a moving average algorithm was used. These time-dependent spectra were used to quantify the diffusion coefficients of agents in the skin using an algorithm detailed in [46, 47]. In addition to measuring the thickness of the samples (Table 2), which is necessary for the algorithm to work correctly, their weight was measured using a digital balance (Scientech, USA) with an accuracy of 1 mg before and after 60 min of exposure to the agent. The data were averaged over three to five measurements, which is important for taking into account water losses during the immersion process when interpreting the measurement results.

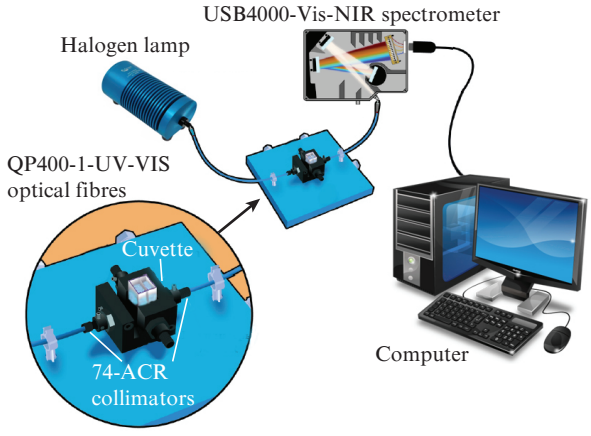

Figure 5. Experimental setup for measuring collimated transmission spectra of skin samples *ex vivo* placed in contrast MRI or CT agents [45].

The effective diffusion coefficients D_a^{tissue} of the OCA in mouse skin were calculated using the time dependences of the collimated transmission coefficient $T_c(t)$ [47]:

$$T_c(t) \propto 1 - \exp(-t/\tau), \tag{2}$$

$$\tau = \frac{4l^2}{\pi^2 D_a^{tissue}}, \tag{3}$$

where τ is the characteristic diffusion time of the agent during its delivery, preferably through one of the surfaces of the sample, i.e., through the dermis of the skin, which is more permeable than the stratum corneum and epidermis; the sample thickness l is much less than its area.

Diffusion of molecules in tissues can be considered as a process that is impeded by cells and fibrous tissue structures, which leads to an increase in the path length of molecules caused by their interaction with these obstacles. This diffusion in tissues, which is hindered compared to diffusion in a homogeneous medium (water or a very dilute gel), as well as in tissue interstitial fluid (ISF), is quantitatively determined by the tortuosity of the tissue structure [48–50]:

$$\frac{l_d}{L} = \sqrt{\frac{D_a^{free}}{D_a^{tissue}}}, \tag{4}$$

where D_a^{free} is the agent diffusion coefficient in a homogeneous liquid free of inclusions; and D_a^{tissue} is the effective diffusion coefficient, taking into account the lengthening of its path. The tortuosity is a measure of the geometric complexity of a porous medium, such as biological tissue, and it can be represented as the ratio of the molecular flow path length between two points l_d to the direct distance L between these points [51].

With the help of Eqn (2), the efficiency of OC (EOC) η can be introduced, which is defined as the ratio of the collimated transmission coefficient T_c^{OC} after the completion of the OC process to its initial value ?T_c^0

$$\eta = T_c^{OC}/T_c^0. \tag{5}$$

The transmission of a narrow collimated light beam through a thin layer of tissue l is described by the Bouguer–Beer–Lambert law [3]:

$$T_c = I(l)/I_0 = \exp(-\mu_t l), \tag{6}$$

where I_0 and $I(l)$ are the intensities of the incident and transmitted light, respectively; and

$$\mu_t = \mu_a + \mu_s \tag{7}$$

are the coefficients of light extinction (attenuation), absorption and scattering, respectively. For soft tissues in the visible and NIR ranges $\mu_s \gg \mu_a$.

For many soft tissues, consisting of Mie scatterers, for which the scattering anisotropy factor $g \geqslant 0.9$, the diameter $2a$ and the relative refractive index (RI) $m = n_s/n_0$ lie in the ranges $5 < 2\pi a/\lambda < 50$ and $1 < m < 1.1$, respectively, the scattering coefficient is expressed as [52, 53]

$$\mu_s = \frac{3.28\pi a^2}{1-g}\rho_s\left(\frac{2\pi n_0 a}{\lambda_0}\right)^{0.37}(m-1)^{2.09}, \tag{8}$$

where ρ_s is the volume density of the scatterers; λ_0 is the wavelength of the incident light; and n_s and n_0 are the RIs of the scatterers and the environment (e.g., collagen fibres and ISF), respectively.

In general, it is necessary that the RI in OCA be higher than that of ISF, and as close as possible to the RI of hard tissue components (scatterers), such as conglomerates of proteins, lipids, etc. [3, 27, 29, 30]. Typically, the ISF has n = 1.35–1.36 for λ = 400 nm and 1.33–1.34 for λ = 1000 nm)

[27, 52, 54], which is close to the RI of water, which varies from 1.34 (λ = 400 nm) to 1.33 (λ = 1000 nm) [55].

To make sure that the investigated agents can provide the required OC efficiency, we will make estimates using the Gladstone–Dale formula for the RI of a two-component mixture and literature data for RI of the components of biological tissues and their volume fractions [8, 27]. In particular, for RI of the skin n_{skin} in the model of a mixture of ISF (with a fraction of f_{ISF} and RI n_{ISF}) and a hydrated solid (protein) component of the skin dermis (with a fraction of $1 - f_{ISF}$ and RI $n_{protein}$) we have

$$n_{skin} = n_{ISF} f_{ISF} + n_{protein}(1 - f_{ISF}). \quad (9)$$

Assuming $f_{ISF} = 0.5$ and using the known data for n_{skin} [3], we obtain $n_{protein}$ = 1.44 (λ = 400 nm) and 1.41 (λ = 1550 nm). For skeletal muscle tissue of rats, $n_{protein}$ = 1.56 (λ = 400 nm) and 1.51 (λ = 1000 nm) [27, 54], and for the mucous membrane of the human colon, $n_{protein}$ = 1.377 (λ = 400 nm) and 1.343 (λ = 1000 nm) [27, 52]. These data make it possible to determine the required value of the RI of the used OCA and associate it with the EOC [Eqn (5)].

From Eqn (8), it follows that the tissue scattering coefficient is very sensitive to changes in the relative RI m, which changes during tissue immersion in the OCA. If we assume that for the initial (non-cleared) state of a tissue sample with thickness l, $\mu_s l$ = 2, then, taking into account that $\mu_s \gg \mu_a$, the coefficient of the initial collimated transmission of the sample is calculated using Eqn (6) as $T_c^0 = 0.14$. If it is necessary to obtain η = 2.6 [Eqn (5)], i.e., to increase the transmittance to T_c^{OC} = 0.37, then $\mu_s l = 1$ must be ensured.

To estimate the RI of the OCA that can provide such an efficiency, let us consider as an example the data for the human colon membrane [52], for which the initial values of the relative RI before clearing are m = 1.019 (400 nm) and m = 1.013 (1000 nm). From Eqn (8), it is easy to obtain that after clearing

$$m_{OC} \approx 1 + (m - 1)/\sqrt{2}, \quad (10)$$

i.e., m_{OC} = 1.0135 (400 nm) and 1.009 (1000 nm). According to [52], $n_s = n_{protein}$ = 1.377 (400 nm) and 1.343 (1000 nm), and n_0 = 1.351 (400 nm) and 1.325 (1000 nm). Upon clearing, the RI of the ISF changes from n_0 to

$$n_0^{OC} = n_0 f_{ISF} + n_{OCA}(1 - f_{ISF}), \quad (11)$$

where f_{ISF} is the volume fraction of the initial ISF; $1 - f_{ISF}$ is the volume fraction of OCA penetrating into the tissue; and n_{OCA} is its RI. For equal volume fractions of ISF and OCA, f_{ISF} = 0.5, then to obtain η = 2.6 it is necessary that n_{OCA} = 1.367 (400 nm) and 1.337 (1000 nm). It is easy to see that all the agents whose RIs are shown in Fig. 1 can provide such and even greater efficiency.

Figure 6 shows the dependences of the collimated transmission coefficients at a number of wavelengths for the skin

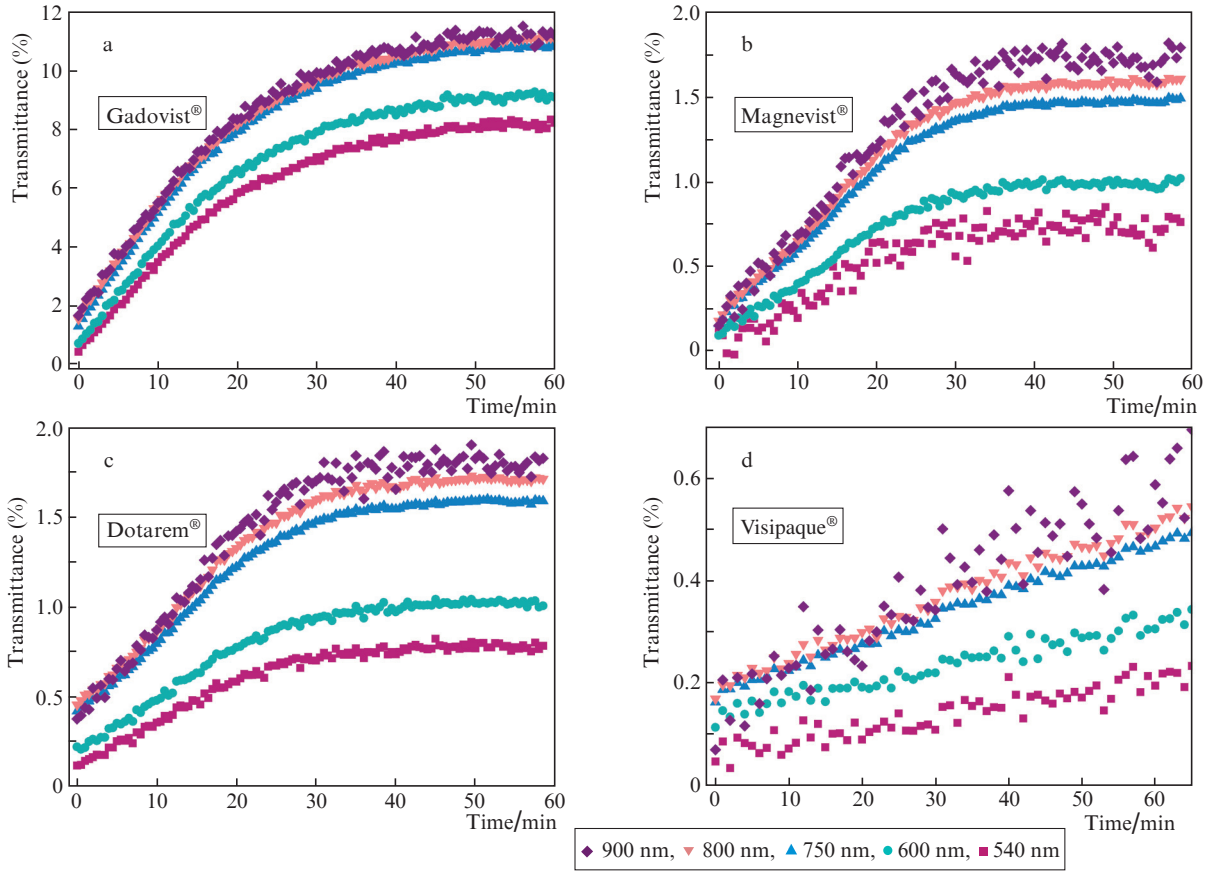

Figure 6. Dependences of the collimated transmission coefficients of Nu/Nu mice skin samples on the time of action of the contrast MRI agents Gadovist® (a), Magnevist® (b), and Dotarem® (c), as well as of the skin samples of white mice on the time of action of the contrast CT agent Visipaque® (d).

Table 3. Optical clearing efficiency [Eqn (5)] of the murine skin after 60 min of exposure to contrast MRI agents (Nu/Nu mice) and a contrast CT agent (white mice).

Wavelength/nm	$\eta = T_c^{OC}/T_c^0$			
	MRI agents			CT agent
	Gadovict®	Magnevist®	Dotarem®	Visipaque®
540	18.87 ± 0.19	8.99 ± 0.18	6.85 ± 0.17	3.54 ± 1.09
600	12.56 ± 0.14	9.18 ± 1.30	4.74 ± 0.28	2.34 ± 0.24
750	8.29 ± 0.04	9.11 ± 0.07	3.80 ± 0.02	2.61 ± 0.18
800	7.21 ± 0.01	9.00 ± 0.20	3.78 ± 0.03	2.69 ± 0.19
900	6.73 ± 0.04	10.60 ± 0.81	4.48 ± 0.05	4.08 ± 0.75

samples of white and Nu/Nu mice on the time of their immersion in various agents. The data illustrating the EOC [Eqn (5)] of the mouse skin at individual wavelengths after 60 min of immersion are summarised in Table 3.

The coefficients of collimated transmission of mouse skin in the spectral range of 540–900 nm increase significantly, almost up to 19 times, with a gradual saturation of their time dependences under conditions of continuous exposure of the samples to agents for 30–40 min. The best result was obtained for Gadovist® (Fig. 6a, Table 3) for wavelengths of 540–600 nm. The transmittance of mouse skin samples at a wavelength of 540 nm increased by 8 times after the first 10 minutes and almost by 19 times after 60 minutes of incubation in Gadovist®. For a longer wavelength (λ = 600 nm), the use of Gadovist® increased the transmittance by 5.6 times during the first 10 min and by 12.6 times during 60 min of exposure. It is important to note that during the OC, no changes were found in the geometry or weight of the sample, which retained a constant thickness of 0.27 mm and a weight of 94 mg (Table 4).

The action of Magnevist® on the skin during 60 min also produced a significant OC with an increase in the transmittance by a factor of 9–10 for all wavelengths (Fig. 6b, Table 3). It is important to note that at longer wavelengths Magnevist® proved to be more effective than Gadovist®. This fact may be due to the influence of an additional clearing mechanism, namely, partial tissue dehydration caused by Magnevist® (Fig. 6b, Tables 2–4), which is an ionic agent with a linear ligand structure and a higher osmolarity than Gadovist® [56–65].

Exposure to Dotarem® also leads to a high EOC level with an increase in the transmittance in the first 10 min by 3 times and almost 7 times in 60 min at a wavelength of 540 nm (Fig. 6c, Table 3). Exposure to Visipaque® produces the smallest increase in skin optical transmission compared to other agents (Fig. 6). Nevertheless, the EOC for it is also quite high and amounts to 3.5–4.0 for all wavelengths (Table 3). For wavelengths above 600 nm, both Dotarem® and Visipaque® have close EOC values, which are about half that of Gadovist® or Magnevist®. For Visipaque®, the transmittance is not as high as for Dotarem® because, as shown in Fig. 6, the initial transmittance of a skin sample immersed in Visipaque® is less than in the experiment with Dotarem®. In the control experiment, i.e., for the sample immersed in saline, only a slight decrease in the transmittance was observed over time due to tissue swelling.

The initial coefficient of collimated transmission of tissue samples is much lower for shorter wavelengths [see Eqns (6)–(8)] due to the stronger light scattering [3], which leads to a higher OC efficiency at these wavelengths.

To determine the diffusion coefficient based on kinetic curves (Fig. 6) using relations (2) and (3), the thickness and weight of the skin samples were measured before and after immersion in solutions. Table 4 shows the average values of these parameters. The effect of Gadovist® does not change the thickness and weight of the samples, Magnevist® and Dotarem® also have little effect on the thickness of the samples, but lead to their slight shrinkage (Magnevist®) or swelling (Dotarem®), which is expressed in a slight decrease or increase in their weight, respectively (Table 4). Differences in volumetric and transverse shrinkage/swelling [47] may be associated with differences in molecular structure (linear or macrocyclic), osmolarity and pH of agents [56–65], to which collagen structures are sensitive because of their tendency to shrink or swell [66, 67]. Some transverse and volumetric swelling of the skin samples was found under the action of Visipaque®. Note that in order to avoid strong swelling of tissue samples when using agents, the exposure time should not exceed 60 min [68].

The main physicochemical properties of MRI contrast agents can be found in Refs [56–65]. The absence of charge in the case of non-ionic agents (Gadovist®) as compared to ionic agents (Magnevist® and Dotarem®), as well as their osmolarity, should potentially affect OC efficiency and diffusion kinetics. According to the obtained kinetic data, Gadovist® demonstrated a better ability to OC, which is also expressed in an increase in the optical transmittance of skin 0.27 mm

Table 4. Results of measurements of thickness (l_0, l) and weight (w_0, w) of mouse skin samples before (l_0, w_0) and after (l, w) immersion in MRI and CT agents for 60 min.

Agents	l_0/mm	l/mm	w_0/mg	w/mg
Gadovict®	0.27 ± 0.02	0.27 ± 0.02	94 ± 9	94 ± 8
Magnevist®	0.35 ± 0.05	0.37 ± 0.10	130 ± 25	118 ± 30
Dotarem®	0.32 ± 0.05	0.32 ± 0.05	96 ± 10	102 ± 8
Visipaque®	0.34 ± 0.07	0.39 ± 0.07	70 ± 2	75 ± 2
Saline	0.27 ± 0.02	0.32 ± 0.02	84 ± 2	105 ± 2

Note. The thickness measurements were carried out using a digital micrometer (Fujisan, China). The data correspond to the results of spectral measurements shown in Fig. 6.

thick approximately by 3.5–4 times at wavelengths 750–900 nm 10 min after the beginning of the agent action (Fig. 6). The use of Magnevist® showed approximately the same increase in transmittance at these wavelengths during the first 10 min, but led to a greater effect than in the case of Gadovist®, under prolonged (60 min) action of the agents (see Table 3).

Using the algorithm described by Eqns (2) and (3), the effective coefficients D_a^{tissue} of contrast agents diffusion in the murine skin were found (Table 5) from the kinetic curves $T_c(t)$ in Fig. 6 and with the data on the samples thickness from Table 4 taken into account. It is important to compare the data obtained with the measured diffusion coefficients of MRI contrast agents in other tissues. Typically, such a comparison is made using data for D_a^{free}, i.e., the diffusion coefficient of an agent in a homogeneous medium such as water or ISF [48–50].

Table 5. Effective coefficients of diffusion D_a^{tissue} in the mouse skin tissue for MRI (Nu/Nu mice) and CT contrast agents (white mice), extracted from the measurements of the collimated transmittance kinetics (Fig. 6) and sample thicknesses $l \equiv L$ (Table 4), as well as the estimated structural tortuosity paramete l_d/L of the of mouse skin.

MRI agents	CT agent	D_a^{tissue}/cm^2 s^{-1}	D_a^{free}/cm^2 s^{-1}	l_d/L
Gadovist®		$(4.29 \pm 0.39) \times 10^{-7}$	3.9×10^{-6}	3.0
Magnevist®		$(5.00 \pm 0.72) \times 10^{-7}$	–	–
Dotarem®		$(3.72 \pm 0.67) \times 10^{-7}$	4.5×10^{-6}	3.5
	Visipaque®	$(1.64 \pm 0.18) \times 10^{-7}$	–	–

Note. Averaging was performed for all kinetic curves from 500 to 900 nm. The data for the free diffusion coefficient D_a^{free} were taken from [49, 50].

Diffusion of molecules in tissues is a free diffusion process impeded by tissue structures. In this regard, there is an increase in the path length of the molecule to l_d in comparison with the path length L in the free medium, which is quantitatively determined by Eqn (4) as the parameter of the tortuosity of the tissue structure l_d/L. For Dotarem®, $D_a^{free} = (5.18 \pm 1.18) \times 10^{-6}$ cm^2 s^{-1} at room temperature. It was recalculated for a physiological temperature of 37 °C and amounted to $(7.96 \pm 1.82) \times 10^{-6}$ cm^2 s^{-1} [49]. According to [50], $D_a^{free} = 3.9 \times 10^{-6}$ cm^2 s^{-1} for Gadovist® and 4.5×10^{-6} cm^2 s^{-1} for Dotarem®. These values were used to estimate the parameter of the structural tortuosity of the skin based on the measured effective diffusion coefficients presented in Table 5. The value of the tortuosity parameter determined in this way $l_d/L = 3–3.5$ for the skin is quite acceptable in comparison with rat brain tissues more permeable to molecules with an estimated structural tortuosity of 1.2–1.6 [48–50]. Note that the effective diffusion coefficients of MRI agents in the skin of mice obtained in this work are higher than those of the Visipaque® CT agent. In particular, the measured diffusion coefficient for Dotarem® is approximately twice that for Visipaque®, which is in good agreement with the ratio of their molecular masses 753.9/1550.2 [56–65], as follows from the dependence of the diffusion coefficient on the molecular mass of the agent during diffusion in muscle fibre preparations [69].

5. Investigation of the OC effect on the fluorescence of experimental tumours

To obtain xenografts, Nu/Nu nude mice were used. Adhesive culture of human laryngeal adenocarcinoma cells HEp2, stably expressing the TagRFP protein, was grown in a culture flask in an RPMI-1640 medium (Paneco, Russia) supplemented with 10% fetal bovine serum (Bioclot, Germany) up to 70% confluence, then removed with trypsin, washed and resuspended in cold Dulbecco's phosphate buffered saline (DPBS) (10^6 cells in 100 μL of DPBS). The cell suspension was injected subcutaneously into the right flank of the animals [70].

Fluorescence images of mouse tumour xenografts were obtained using a Nikon Eclipse TE2000-U microscope equipped with a DCS-120 confocal scanning system (Becker & Hickl GmbH, Germany), a WL-SC-480-6 Supercontinuum laser, and an AOTF-V1-DFDS acousto-optical tunable filter -SM (Fianium, Great Britain), as well as a hybrid detector HPM-100-40 (Becker & Hickl GmbH, Germany) (Fig. 7). The fluorescence was recorded using a DCS-120 system, to which a light signal was directed through a quartz beam splitter plate, as well as low-pass (HQ 550LP Chroma) and bandpass (580BP40 Omega) filters for separating excitation and fluorescence signals. The DCS-120 system is based on the multidimensional time-correlated single photon counting (TCSPC) method described in Ref. [71]. For measurements, the intensity mode (integral signal) of TCSPC was used, which gives a gain in sensitivity due to background suppression, since only the photons correlated with the flash are counted rather than all photons arriving at the PMT.

The test animal was anesthetised by intramuscular (IM) injection using a 1:1 mixture of Zoletil 50 (Virbac, France) and Rometar 2% (Spofa Praha, Czech Republic), and then placed in a standard small animal imaging cassette (FMT4, Perkin Elmer, USA) and positioned on a movable microscope stage (Figs 7c, 7d). Laser radiation with a wavelength of 540 nm was focused on the mouse skin surface after passing through an acousto optic tunable filter, Nikon TRITC EX540/25 nm bandpass optical filters, and a Nikon 2x plan achromatic objective. The fluorescence radiation of the TagRFP-marked tumour was collected through the same objective in the inverted epi-illumination mode configuration (Fig. 7) [70, 72].

Fluorescence images of the mouse tumour xenograft were recorded before OC, immediately after OC, and then again 1 hour later. After obtaining the first control image, the cassette with the animal was opened and OC was performed by applying OCA to the tumour area using a thin cotton swab preimpregnated with OCA (Gadovist®, 1 mmol mL^{-1}, Bayer HealthCare Pharmaceuticals, Germany) during 15 min. After OC, the cassette with the animal was carefully closed and returned to the movable stage to obtain the second image (immediately after OC). The settings of the measuring system ensured practical coincidence of the coordinates of the first and second images. The next images were recorded every 15 min for 60 min without opening the cassette. The time of data collection in order to obtain one image for the anesthetised mouse ranged from 1 to 2 min (depending on the level of fluorophore expression). Fluorescence images were analysed using the NIH ImageJ 1.48v software.

An *in vivo* study aimed at verifying the effectiveness of OC using the Gadovist® MRI contrast agent applied to the skin of Nu/Nu nude mice was performed using an implanted subcutaneous tumour and measuring the fluorescence intensity profiles of the TagRFP marker expressed in HEp2-TagRFP tumour cells.

The images obtained in the form of the TagRFP fluorescence intensity distribution, presented in Fig. 8, well demon-

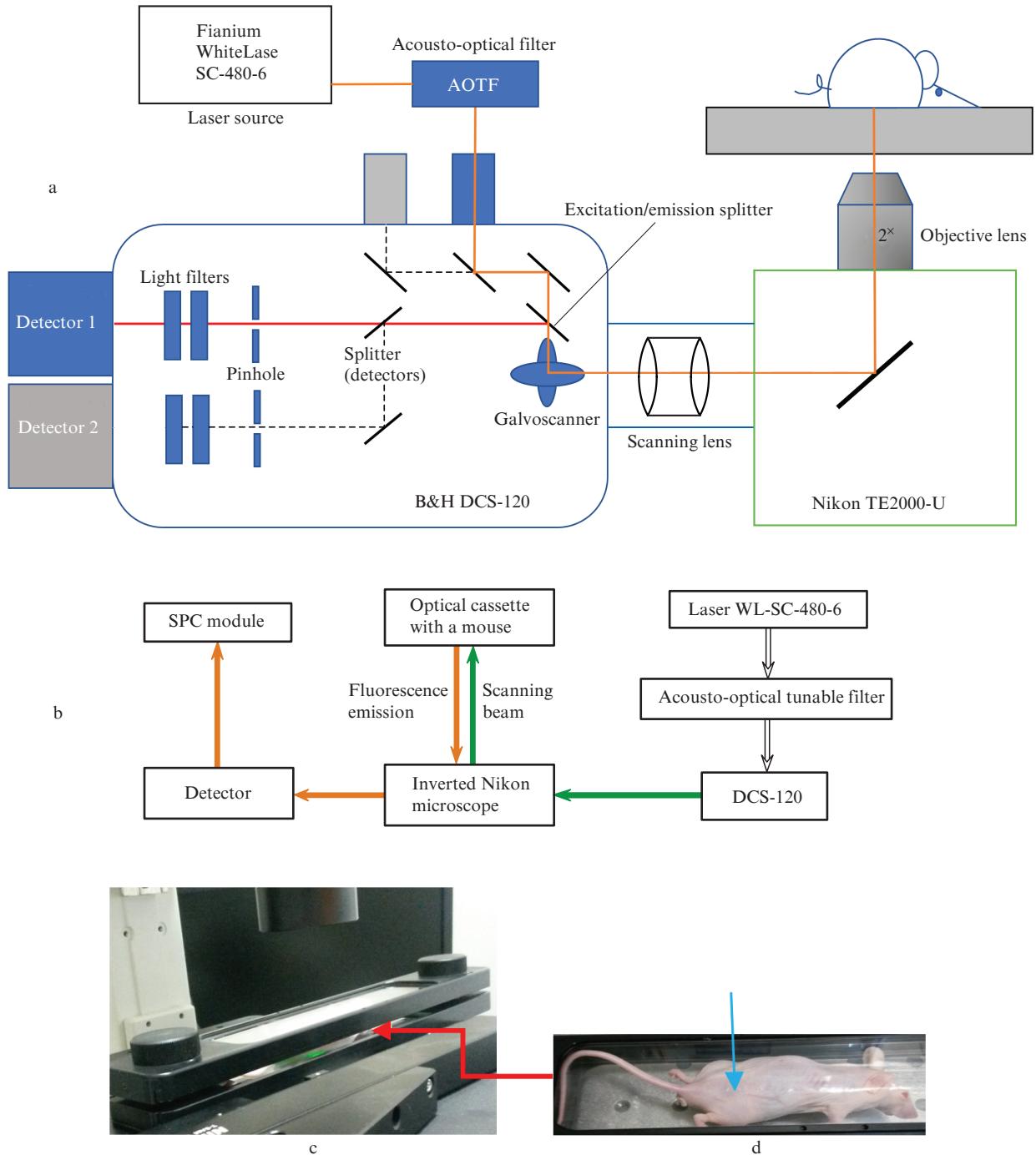

Figure 7. Schematic diagram of the experimental setup for visualising the distribution of fluorescence intensity with additional detector 2 used for simultaneous studies at a second wavelength (a); functional diagram of the experimental setup (b); movable microscope stage with a cassette containing an animal (c); scaled up image of a mouse inside the cassette; the arrow points at the tumour xenograft (d).

strate the high efficiency of the clearing effect of the MRI contrast agent Gadovist® in *in vivo* studies. These images were recorded before the OC, 15 min and 1 hour after the OC. The details of the fluorescence intensity profile along the line in the tumour image are shown in Fig. 9. The same Figure shows the distribution of the ratio of the fluorescence intensity to the initial value of the profile measured at the same points, which was evaluated immediately and 1 hour after the OC (Fig. 9b). The distribution of this ratio was also analysed depending on the initial level of tumour fluorescence (Fig. 9c). This allows establishing the tendencies of changes in the fluorescence intensity during the experiment. For tumour areas with average or low intensity of initial fluorescence (these are small tumour nodes or the peripheral region of a tumour), OC causes a significant, almost twofold, increase in the intensity of tumour fluorescence in the region of coordinate 0.5 immediately after application of OCA (Fig. 9a). An hour after OC, the fluorescence intensity of the tumour is already more than 3 times higher than the initial level. This is in good agreement with the data in Table 3 for the efficiency of *ex*

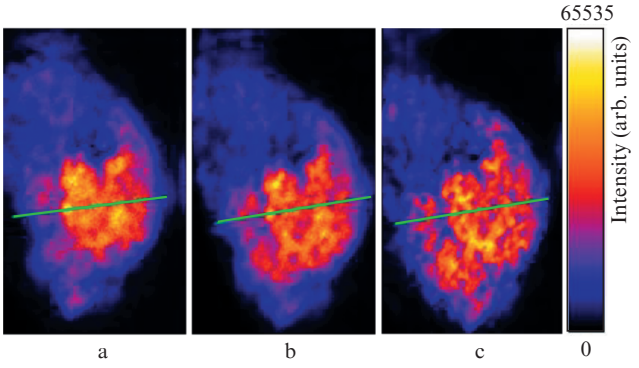

Figure 8. (Colour online) Distributions of fluorescence intensity in the subcutaneous xenograft of the HEp2-TagRFP tumour before (a), immediately after (b) and 1 h after (c) topical application of the Gadovist® contrast MRI agent. The wavelength of the exciting light is 540 nm. The fluorescence intensity was measured in the spectral region of 560–600 nm, each image was acquired for about 2 min. The images are pseudo-coloured using the ImageJ program.

vivo skin clearing, taking into account the differences in the method of the agent application, the time of its action and the method of optical measurements. It is important that even 1 hour after application of the agent to the skin, it continued to act, providing a better signal-to-noise ratio and image contrast of tumour nodes. The maximum possible clearing efficiency reaches 7–9 times (Fig. 9c), which is in good agreement with the data of *ex vivo* measurements (see Table 3).

In the case of medium levels of the initial tumour fluorescence intensity, the fluorescence intensity in the non-peripheral region increased up to 1.5 times immediately after the OC, with even greater increase observed 1 hour after the OC (Fig. 9c). Such differences in the distribution of fluorescence intensity after OC in areas with initially lower intensity can be explained by different rates of OCA diffusion in the central and peripheral regions of the tumour, different density of tissues and tumour vasculature. In the case of a higher initial fluorescence intensity in the central areas of the tumour, the fluorescence intensity under the action of the agent does not increase so much (Fig. 9a).

An increase in the contrast of the fluorescence image is clearly seen in another example shown in Fig. 10, which demonstrates the distributions of the fluorescence intensity from a tumour fragment in the region of a blood vessel of another mouse with a more developed tumour [73]. The data in Fig. 10 allow evaluating the contrast of the vessel image and its apparent diameter before and after OC. To estimate contrast K we used Eqn (1). The apparent diameter of the vessel was determined as the full width at half maximum (FWHM) of the intensity profiles along the black lines in Figs 10a–10c, presented in Fig. 10e. It turned out that before the OC, the measured diameter of the vessel was about 200 μm, and the contrast of its image was $K = 0.14$. After 15 min of OC, the visible vessel diameter became 140 μm with good contrast, $K = 0.67$. This 4.8-fold increase in contrast with the application of Gadovist® agent is in good agreement with the improvement in contrast obtained for the murine skin *ex vivo* in the model experiment shown in Fig. 2 and Table 1. An hour after the OC, the optical properties of the skin partially returned to the initial levels of scattering and fluorescence due to washing out of the OCA from the skin of a living mouse. The contrast of the image decreases to 0.27, and the apparent diameter of the vessel increases to 180 μm. Typically, it takes several hours for the complete termination of OCA action [8].

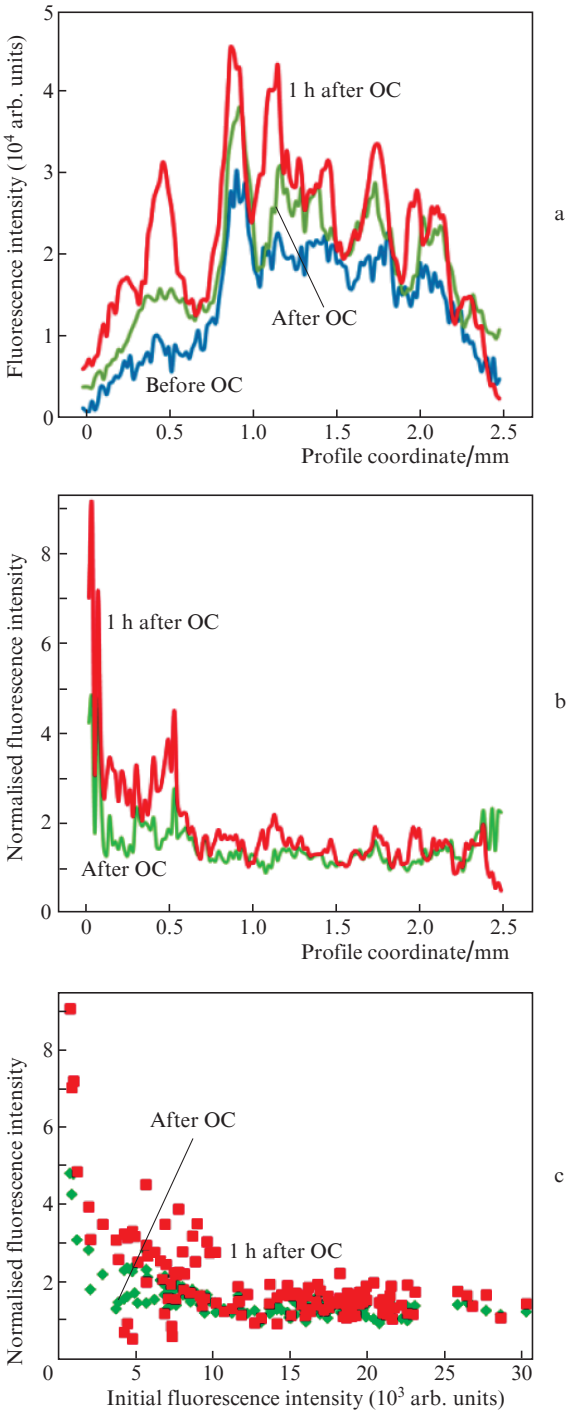

Figure 9. (Colour online) Distributions of the fluorescence intensity of the HEp2-TagRFP tumour node along the lines shown in Fig. 8 before OC, immediately after OC, and 1 h after OC: fluorescence intensity profiles (a), profiles normalised to the initial fluorescence intensity immediately and 1 h after OC (b), and normalised fluorescence intensity versus initial intensity for the same profiles (c).

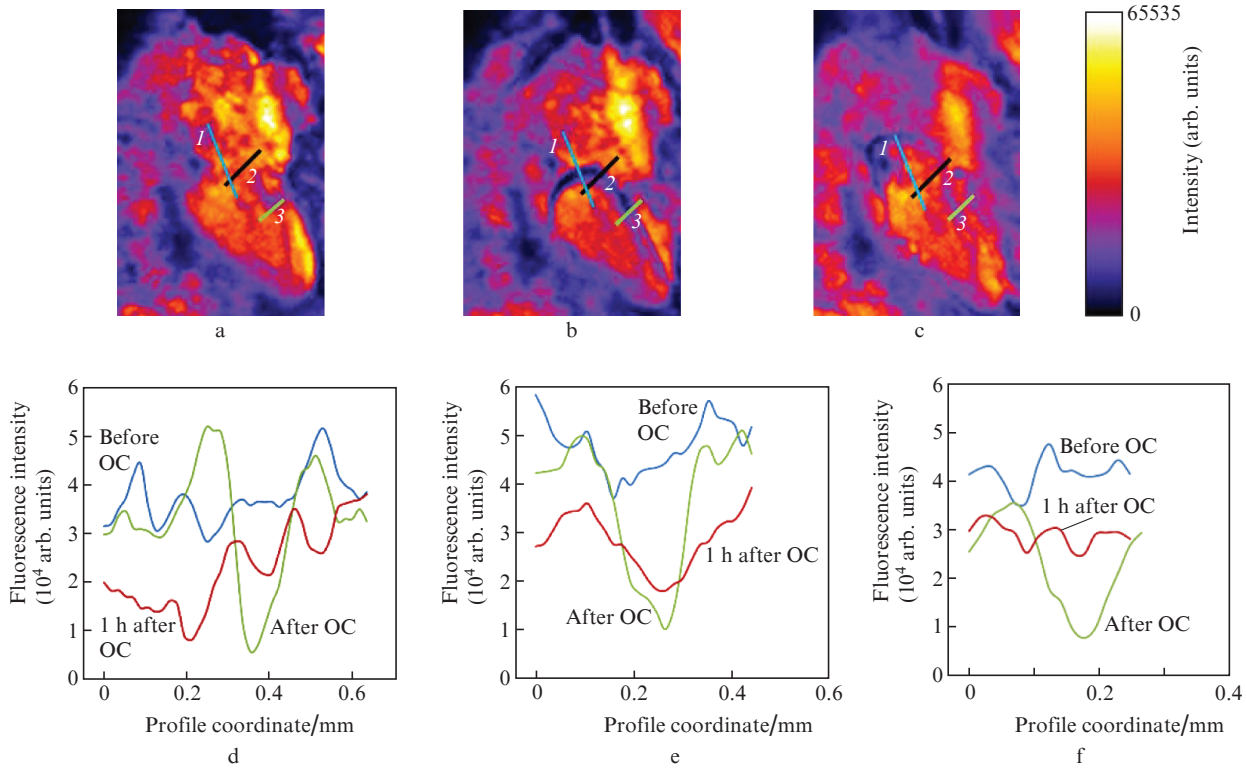

Figure 10. (Colour online) Distributions of fluorescence intensity from a tumour node near a blood vessel before optical clearing (a), after 15 minutes of clearing with the contrast MRI agent Gadovist® (b) and 1 hour after the end of clearing (c); profiles of the distribution of fluorescence intensity along the blue 1 (d), black 2 (e) and green 3 (f) lines in the images (a), (b) and (c).

Generally, *in vivo* studies confirm the idea that the efficiency of OC is much higher in the case of initially lower fluorescence intensity. As follows from Fig. 9c, for low intensities the maximum OC efficiency is 2–9, which is in good agreement with the trend observed in *ex vivo* studies (see Table 3).

No signs of any systemic toxicity (including behavioural changes) were observed in the studied animals after topical application of the Gadovist® MRI contrast agent with a concentration of 1 mmol mL^{-1}. In addition, no hyperaemia of the tissue surrounding the mouse tumour was observed during the OC procedure and within 24 h after OC. There were no signs of inflammation in the area of tumour tissue exposed to OC during and after the exposure.

6. Discussion of results

In the present study, several clinically available MRI and CT contrast agents were investigated to determine their efficiency for optical clearing of skin *ex vivo* and i*n vivo*. In *in vitro* studies with chemical fixation of biological tissues, the relative volume fractions of their components undergo significant changes; in addition, intra- and intermolecular cross-links occur, which significantly distort the diffusion properties of tissues, slowing down the rate of diffusion of molecules [74, 75]. In this regard, all studies in this work were carried out on fresh tissues *ex vivo* or *in vivo*.

The main motivation for the study was that the existing OC protocols developed for optical imaging have not yet been applied for multimodal imaging of tissues and organs, e.g., in combination with MRI, CT or Cherenkov-excited luminescence sheet imaging (CELSI) [76], as well as with other methods, potentially offering a variety of possibilities for visualising both structural and functional features of normal and pathological tissues and organs with high anatomical resolution and molecular specificity. A clinically approved iodine-based isoosmolar CT contrast agent, iodixanol (1550.19 g mol^{-1}) (Visipaque®), was included in this study due to its efficacy as an MRI contrast agent, which has recently allowed testing for bimodal CT/MRI visualisation using iodixanol-loaded liposomes [42].

In addition to evaluating the efficiency of OC using contrast MRI and CT agents, the data obtained are important for clinical endoscopic optical studies in combination with MRI or CT, i.e., for multimodal diagnostic schemes.

Measurements of the refractive indices of all selected agents showed that they are all high enough to provide skin OC in the entire spectral range selected for testing (see Fig. 1). Gadovist® was shown to have a greater clearing effect, assessed by both OCT imaging and collimated transmittance measurements. In addition, unlike other agents, incubation of skin samples in Gadovist® did not result in tissue swelling or shrinkage, and a pilot study using a tumour xenograft expressing the fluorescent TagRFP protein showed excellent optical clearing properties of Gadovist® *in vivo*.

The observed lower OC efficiency achieved *ex vivo* in the case of the isoosmolar CT agent Visipaque® may be due to the relatively high molecular weight of iodixanol (1550.19 g mol^{-1}) compared to about 50% less mass of iohexol molecules (821.14 g mol^{-1}), the previously tested

iodine-containing Omnipaque® CT agent. The latter has been reported to improve the optical transparency in a number of tissues [20, 23, 27, 34–37] and can also potentially be used instead of Visipaque® for CEST imaging [42]. Although the efficiency of OC with Visipaque® was not as high as in the case of MRI agents, the concept of tri-modal MRI/CT/optical tissue imaging using iodine-based CT contrast agents could be proposed based on the data obtained in this study.

It is important to note that a simple and reliable optical method based on the concept of the free diffusion coefficient [48–50] made it possible to measure the diffusion coefficients of MRI agents in the skin of mice and compare their values with those measured in other tissues using MRI. Such a comparison made it possible to estimate the parameter of tortuosity of the murine skin structure at the level of 3–3.5, which is quite acceptable for a tissue with barrier function [66].

Pilot *in vivo* studies in tumour xenografts expressing the red fluorescent protein TagRFP showed that the fluorescence intensity significantly increases after optical clearing with the Gadovist® MRI agent, thereby demonstrating good prospects for the use of contrast MRI agents in optical imaging and in combination with MRI.

When using the MRI agent Gadovist® *in vivo*, an almost five-fold increase in the contrast of the fluorescence image of the vessels in the tumour area was observed, which is in good agreement with the contrast improvement observed in mouse skin *ex vivo*. The increased contrast of the fluorescence image allowed realistic estimation of the diameter of the initially hidden vascular structure. The concept of high efficiency of OC for initially lower fluorescence intensity found a successful confirmation in both ex vivo and in vivo studies.

Multimodal technologies for visualisation of biological tissues using optical and CT/MRI methods have obvious limitations due to the physical principles of each of the methods. For example, optical methods do not allow imaging of the whole body or a single large organ, but they can visualise pathology of the brain, breast, finger joints, and hollow organs (using endoscopes). In all these cases, optical clearing helps to reduce scattering and obtain a better optical image [3, 33, 77, 78]. The technology of injection of an agent for multimodal imaging should correspond to the tasks to be solved. For example, for OCT/MRI/CT studies of superficial organs, it will be sufficient to inject the agent locally [60, 79–81]; for combined imaging of deeper tissues, interstitial/intraorganic injection or combined topical and interstitial administration can be used [79, 82, 83]. Oral administration is also possible, and not only for the study of the gastrointestinal tract, but also for saturating other organs having pathology with a contrast/clearing agent (as an alternative to intravenous injection) [79, 82–85].

7. Conclusions

This paper is the first to describe the optical and diffusion properties of contrast MRI agents and discuss their potential in terms of optical clearing of biological tissues, which has been demonstrated using digital microscopy, OCT, spectral collimated transmittance measurements and fluorescence imaging. The new data from the skin of mice could potentially be important for preclinical and clinical studies that use MRI in combination with optical imaging. Therefore, contrast MRI agents (based on gadolinium) can not only increase the contrast of MRI images of tissues and organs, but also effectively reduce the scattering of optical radiation by biological tissues, which leads to an increase in the contrast and depth of probing of optical methods and, ultimately, opens perspective of using multimodal diagnostics with a single agent. In addition, such agents are able to enhance the fluorescence intensity of molecular markers expressed in tumours *in vivo*.

Since several contrast CT agents can also provide increased contrast of optical and MRI images, the results of our study open the way to a fundamentally new approach to multimodality, including optical, MRI and CT imaging synchronised in time and space. This is because the same agent is able to increase simultaneously the contrast of all three imaging methods.

Optical methods, the efficiency of which can be significantly increased by means of optical clearing using contrast MRI agents, are not limited to spectral, OCT and fluorescence imaging, but also include confocal microscopy, Raman spectroscopy, multiphoton microscopy, photoacoustic imaging, etc.

Acknowledgements. The work of D.K. Tuchina and V.V. Tuchin was supported by the Russian Foundation for Basic Research (Grant No. 18-52-16025-NTsNIL_a), and the work of O.A. Sindeeva on the preparation of animal tissue samples for spectral and OCT measurements was supported by the Russian Science Foundation (Project No. 19-75-10043).

The authors are grateful to Professor Luis M. Oliveira for assistance in processing collimated transmission spectra, to Dr. Teemu Myllylä for providing the Visipaque® agent, and to postgraduate student S.M. Zaitsev for help in preparing documents for the approval of animal studies by the Ethics Committee.

References

1. Akselrod-Ballin A., Dafni H., Addadi Y., Biton I., Avni R., Brenner Y., Neeman M. *Sci. Rep*., **6**, 27940 (2016).
2. Leitgeb R.A., Baumann B. *Front. Phys*., **6**, 114 (2018).
3. Tuchin V.V. *Tissue Optics: Light Scattering Methods and Instruments for Medical Diagnostics* (Bellingham: SPIE, 2015) p. 88.
4. Tuchin V.V. (Ed.). *Handbook of Optical Biomedical Diagnostics. Light-Tissue Interaction. Methods* (Bellingham: SPIE, 2016) p. 1552.
5. García-Martín M.L., López-Larrubia P. (Eds), in *Preclinical MRI. Methods in Molecular Biology* (New York: Humana Press, 2018) p. 441.
6. Tuchin V.V., Maksimova I.L., Zimnyakov D.A., Kon I.L., Mavlutov A.H., Mishin A.A. *J. Biomed. Opt*., **2**, 401 (1997).
7. Khan M.H., Choi B., Chess S., Kelly K.M., McCullough J., Nelson J.S. *Lasers Surg. Med*., **34**, 83 (2004).
8. Tuchin V.V. *Optical Clearing of Tissues and Blood* (Bellingham: SPIE, 2005) p. 256.
9. Tuchin V.V. *IEEE J. Sel. Top. Quantum Electron*., **13**, 1621 (2007).
10. Genina E.A., Bashkatov A.N., Tuchin V.V. *Expert Rev. Med. Devices*, **7**, 825 (2010).
11. Hama H., Kurokawa H., Kawano H., Ando R., Shimogori T., Noda H., Fukami K., Sakaue-Sawano A., Miyawaki A. *Nat. Neurosci*., **14**, 1481 (2011).
12. Erturk A., Mauch C.P., Hellal F., Forstner F., Keck T., Becker K., Jahrling N., Steffens H., Richter M., Hubener M., Kramer E., Kirchhoff F., Dodt H.U., Bradke F. *Nat. Med*., **18**, 166 (2012).

13. Erturk A., Becker K., Jahrling N., Mauch C.P., Hojer C.D., Egen J.G., Hellal F., Bradke F., Sheng M., Dodt H.U. *Nat. Protoc*., **7**, 1983 (2012).
14. Zhu D., Larin K.V., Luo Q., Tuchin V.V. *Laser Photon. Rev*., **7**, 732 (2013).
15. Susaki E.A., Tainaka K., Perrin D., Kishino F., Tawara T., Watanabe T.M., Yokoyama C., Onoe H., Eguchi M., Yamaguchi S., Abe T., Kiyonari H., Shimizu Y., Miyawaki A., Yokota H., Ueda H.R. *Cell*, **157**, 726 (2014).
16. Richardson D.S., Lichtman J.W. *Cell*, **162**, 246 (2015).
17. Genina E.A., Bashkatov A.N., Sinichkin Yu.P., Yanina I.Yu., Tuchin V.V. *J. Biomed. Photon. Eng.*, **1**, 22 (2015).
18. Pan C., Cai R., Quacquarelli F.P., Ghasemigharagoz A., Lourbopoulos A., Matryba P., Plesnila N., Dichgans M., Hellal F., Erturk A. *Nat. Meth*., **13**, 859 (2016).
19. Zhao Q., Dai C., Fan S., Lv J., Nie L. *Sci. Rep*., **6**, 34954 (2016).
20. Ke M.-T., Nakai Y., Fujimoto S., Takayama R., Yoshida S., Kitajima T.S., Sato M., Imai T. *Cell Rep*., **14**, 2718 (2016).
21. Perbellini F., Liu A.K.L., Watson S.A., Bardi I., Rothery S.M., Terracciano C.M. *Sci. Rep*., **7**, 5188 (2017).
22. Qi Y., Yu T., Xu J., Wan P., Ma Y., Zhu J., Li Y., Gong H., Luo Q., Zhu D. *Sci. Adv*., **5**, eaau8355 (2019).
23. Bashkatov A.N., Berezin K.V., Dvoretskiy K.N., Chernavina M.L., Genina E.A., Genin V.D., Kochubey V.I., Lazareva E.N., Pravdin A.B., Shvachkina M.E., Timoshina P.A., Tuchina D.K., Yakovlev D.D., Yakovlev D.A., Yanina I.Yu., Zhernovaya O.S., Tuchin V.V. *J. Biomed. Opt*., **23**, 091416 (2018).
24. Kim J.H., Jang M.J., Choi J., Lee E., Song K.-D., Cho J., Kim K.-T., Cha H.-J., Sun W. *Sci. Rep*., **8**, 12815 (2018).
25. Ochoa L.F., Kholodnykh A., Villarreal P., Tian B., Pal R., Freiberg A.N., Brasier A.R., Motamedi M., Vargas G. *Sci. Rep*., **8**, 13348 (2018).
26. Matryba P., Kaczmarek L., Gołąb J. *Laser Photon. Rev*., **13**, 1800292 (2019).
27. Oliveira L.M., Tuchin V.V. *The Optical Clearing Method – A New Tool for Clinical Practice and Biomedical Engineering* (Switzerland AG, Basel: Springer Nature, 2019) p. 177.
28. Wan P., Zhu J., Xu J., Li Y., Yu T., Zhu D. *Neurophoton*., **5**, 035007 (2018).
29. Costantini I., Cicchi R., Silvestri L., Vanzi F., Pavone F.S. *Biomed. Opt. Express*, **10**, 5251 (2019).
30. Inyushin M., Meshalkina D., Zueva L. Zayas-Santiago A. *Molecules*, **24**, E2388 (2019).
31. Tainaka K., Murakami T.C., Susaki E.A., Shimizu C., Saito R., Takahashi K., Hayashi-Takagi A., Sekiya H., Arima Y., Nojima S., Ikemura M., Ushiku T., Shimizu Y., Murakami M., Tanaka K.F., Iino M., Kasai H., Sasaoka T., Kobayashi K., Miyazono K., Morii E., Isa T., Fukayama M., Kakita A., Ueda H.R. *Cell Rep*., **24**, 2196 (2018).
32. Matsumoto K., Mitani T.T., Horiguchi S.A., Kaneshiro J., Murakami T.C., Mano T., Fujishima H., Konno A., Watanabe T.M., Hirai H., Ueda H.R. *Nat. Protoc*., **14**, 3506 (2019).
33. Bykov A., Hautala T., Kinnunen M., Popov A., Karhula S., Saarakkala S., Nieminen M.T., Tuchin V., Meglinski I. *J. Biophoton*., **9**, 270 (2016).
34. Sdobnov A.Yu., Darvin M.E., Lademann J., Tuchin V.V. *J. Biophoton*., **10**, 1115 (2017).
35. Sdobnov A.Yu., Tuchin V.V., Lademann J., Darvin M.E. *J. Phys. D: Appl. Phys*., **50**, 285401 (2017).
36. Alexandrovskaya Yu.M., Evtushenko E.G., Obrezkova M.M., Tuchin V.V., Sobol E.N. *J. Biophot*., **11**, e201800195 (2018).
37. Sdobnov A.Yu., Darvin M.E., Schleusener J., Lademann J., Tuchin V.V. *J. Biophotonics*, **12**, e201800283 (2019).
38. Caravan P., Ellison J., McMurry T., Lauffer R. *Chem. Rev*., **99**, 2293 (1999).
39. Lin S.P., Brown J.J. *J. Magn. Reson. Imaging*., **25**, 884 (2007).
40. Alshowiman S.S., Alswailem A.K., Almohizy O.A., Alfawaz A.A., Ibn Alshaikh A.A. *Int. J. Pharmac. Sci Inv*., **7**, 11 (2018).
41. Pierre V.C., Allen M.J., Caravan P. *J. Biol. Inorg. Chem*., **19**, 127 (2014).
42. Chen Z., Li Y., Airan R., Han Z., Xu J., Chan K.W.Y., Xu Y., Bulte J.W.M., van Zijl P.C.M., McMahon M.T., Zhou S., Liu G. *Quant. Imaging Med. Surg*., **9**, 1579 (2019).
43. Pandit P., Johnston S.M., Qi Y., Story J., Nelson R., Johnson G.A. *Acad. Radiol*., **20**, 430 (2013).
44. Yanina I.Y., Trunina N.A., Tuchin V.V. *J. Biomed. Opt*., **18**, 111407 (2013).
45. Spectrometer Operating Software Installation and Operation Manual, SpectraSuite®, Document Number 000-20000-300-02-201205, 2009.
46. Tuchin V.V. (Ed.), in *Handbook of Optical Sensing of Glucose in Biological Fluids and Tissues* (Boca Raton: CRC Press, 2009) p. 587.
47. Tuchina D.K., Shi R., Bashkatov A.N., Genina E.A., Zhu D., Luo Q., Tuchin V.V. *J. Biophot*., **8**, 332 (2015).
48. Mériaux S., Conti A., Larrat B. *Front. Phys*., **6**, 38 (2018).
49. Hagberg G.E., Mamedov I., Power A., Beyerlein M., Merkle H., Kiselev V.G., Dhingra K., Kubíček V., Angelovski G., Logothetis N.K. *Contrast Media Mol. Imaging*, **9**, 71 (2014).
50. Conti A., Magnin R., Gerstenmayer M., Tsapis N., Dumont E., Tillement O., Lux F., Le Bihan D., Mériaux S., Penna S.D., Larrat B. *Contrast Media Mol. Imaging*, **2019**, 6341545 (2019).
51. https://www.glossary.oilfield.slb.com/en/Terms/t/tortuosity.aspx (viewed on December 20, 2020).
52. Carneiro I., Carvalho S., Silva V., Henrique R., Oliveira L., Tuchin V.V. *J. Biomed. Opt*., **23**, 121620 (2018).
53. Graaff R., Aarnoudse J.G., Zijp J.R., Sloot P.M.A., de Mul F.F.M., Greve J., Koelink M.H. *Appl. Opt*., **31**, 1370 (1992).
54. Oliveira L.M., Carvalho M.I., Nogueira E.M., Tuchin V.V. *J. Biophoton*., **11**, e201700094 (2018).
55. https://refractiveindex.info/?shelf=3d&book=liquids&page=water (viewed on December 20, 2020).
56. Longo D.L., Michelotti F., Consolino L., Bardini P., Digilio G., Xiao G., Sun P.Z., Aime S. *Invest Radiol*., **51**, 155 (2016).
57. Laurent S., Vander Elst L., Muller R.N. *Contrast Med. Mol. Imaging*, **1**, 128 (2006).
58. Scott L.J. *Clin. Drug Invest*., **38**, 773 (2018).
59. https://pubchem.ncbi.nlm.nih.gov/compound/Gadovist (viewed on December 20, 2020).
60. https://pubchem.ncbi.nlm.nih.gov/compound/Magnevist (viewed on December 20, 2020).
61. https://pubchem.ncbi.nlm.nih.gov/compound/Dotarem (viewed on December 20, 2020).
62. https://www.bayer.ca/omr/online/magnevist-pm-en.pdf (viewed on December 20, 2020).
63. https://www.rxlist.com/dotarem-drug.htm (viewed on December 20, 2020).
64. https://www.umassmed.edu/globalassets/radiology/documents/dotarem-info-1.pdf (viewed on December 20, 2020).
65. https://pubchem.ncbi.nlm.nih.gov/compound/Iodixanol; https://www.rxlist.com/visipaque-drug.htm#clinpharm (viewed on December 20, 2020).
66. Surber C., Abels C., Maibach H. (Eds) *pH of the Skin: Issues and Challenges* (Basel, New York: Karger, 2018).
67. Meyer M. *Biomed. Eng. OnLine*, **18**, 1 (2019); https://doi.org/10.1186/s12938-019-0647-0.
68. LaComb R., Nadiarnykh O., Carey S., Campagnola P.J. *J. Biomed. Opt*., **13**, 021109 (2008).
69. Papadopoulos S., Juergens K.D., Gros G. *Biophys. J*., **79**, 2084 (2000).
70. Zherdeva V., Kazachkina N.I., Shcheslavskiy V., Savitsky A.P. *J. Biomed. Opt*., **23**, 035002 (2018).
71. https://www.becker-hickl.com/wp-content/uploads/2019/06/dcs-hb-8ed-v04f.pdf (viewed on December 20, 2020).
72. Sarkisyan K.S., Goryashchenko A.S., Lidsky P.V., Gorbachev D.A., Bozhanova N.G., Gorokhovatsky A.Y., Pereverzeva A.R., Ryumina A.P., Zherdeva V.V., Savitsky A.P., Solntsev K.M., Bommarius A.S., Sharonov G.V., Lindquist J.R., Drobizhev M., Hughes T.E., Rebane A., Lukyanov K.A., Mishin A.S. *Biophys. J*., **109**, 380 (2015).
73. Tuchina D.K., Meerovich I.G., Sindeeva O.A., Zherdeva V.V., Savitsky A.P., Bogdanov A.A. Jr., Tuchin V.V. *J. Biophotonics*, **13**, e201960249 (2020).
74. Jelescu I.O., Budde M.D. *Front. Phys*., **5**, 61 (2017).

75. Singh H., Bishen K.A., Garg D., Sukhija H., Sharma D., Tomar U. *Dent. J. Adv. Stud*., **7**, 51 (2019).
76. Pogue B.W., Feng J., LaRochelle E P., Bruža P., Lin H., Zhang R., Shell J.R., Dehghani H., Davis S.C., Vinogradov S.A., Gladstone D.J., Jarvis L.A. *Nat. Biomed. Eng*., **2**, 254 (2018).
77. Kolesnikova E.A., Kolesnikov A.S., Zabarylo U., Minet O., Genina E.A., Bashkatov A.N., Tuchin V.V. *Proc. SPIE*, **9031**, 90310C (2014).
78. Chang C.-H., Myers E.M., Kennelly M.J., Fried N.M. *J. Biomed. Opt*., **22**, 018002 (2017).
79. Caldemeyer K.S., Stockberger S.M. Jr., Broderick L.S. *Am. J. Roentgenol.*, **171**, 1501 (1998).
80. Atanasijevic T., Bouraoud N., McGavern D.B., Koretsky A.P. *Neuroimage*, **156**, 146 (2017).
81. Zou J., Wang Z., Chen Y., Zhang G., Chen L., Lu J. *World J. Otorhinolaryngol. Head Neck Surg*., **5**, 180 (2020).
82. Xiao Y.-D., Paudel R., Liu J., Ma C., Zhang Z.-S., Zhou S.-K. *Int. J. Mol. Med*., **38**, 1319 (2016).
83. https://www.accessdata.fda.gov/drugsatfda_docs/label/2017/018956s099lbl.pdf (viewed on December 20, 2020).
84. Jacobs K.E., Behera D., Rosenberg J., Gold G., Moseley M., Yeomans D., Biswal S. *NMR Biomed*., **25**, 563 (2012).
85. Iijima K., Oshima T., Kawakami R., Nemoto T. *iScience*, **24**, 101888 (2021).